Acta Mech 232, 3781–3800 (2021)
https://doi.org/10.1007/s00707-021-03022-4

ORIGINAL PAPER

S. I. Kundalwal · V. K. Choyal · Vijay Choyal

Flexoelectric effect in boron nitride–graphene heterostructures

Received: 17 April 2021 / Revised: 22 May 2021 / Accepted: 9 June 2021 / Published online: 9 July 2021

Abstract Hexagonal boron nitride and graphene layers offer an attractive way to build 2D heterostructures as their lattices are well-matched as well as they are isostructural and isoelectronic. In this work, the flexoelectric coefficients of monolayer boron nitride-graphene heterostructures (BGHs) are determined using molecular dynamics simulations with a Tersoff potential force field. This is achieved by imposing the bending deformation to the pristine BN sheet (BNS) and BGHs. Three shapes of graphene domains are considered: triangular, trapezoidal and circular. Overall polarization of BGHs was enhanced when the graphene domain was surrounded by more N atoms than B atoms. This enhancement is attributed to higher dipole moments due to the C–N interface compared to the C–B interface. The flexoelectric response for BGHs with 5.6% of triangular and trapezoidal graphene domains was enhanced by 15.2% and 7.83%, respectively, and reduced by 25% for the circular graphene domain. We also studied the bending stiffness of pristine BNS and BGHs using the continuum-mechanics approach. Our results also reveal that the bending stiffness of BGHs increases compared to the pristine BNS. Moreover, the enhancement in the flexoelectric coefficient and bending stiffness was more significant when the graphene domain breaks the symmetry of BGHs. Our fundamental study highlights the possibility of using BGHs in nanoelectromechanical systems (NEMS) such as actuators, sensors and resonators.

Nomenclature

E	Total energy
E_i	Site energy
V_{ij}	Bond energy
r_{ij}	Distance between atoms i and j
b_{ij}	Bond angle
f_R	Repulsive potential
f_A	Attractive pair potentials
f_C	Cut-off function
R and D	Model specific parameters
R	Radius of curvature
K	Strain gradient/bending curvature
p and q	Curve fitting parameters
L_x	Length along the direction of x
S_z	Bending displacement

S. I. Kundalwal (✉) · V. K. Choyal · V. Choyal
Applied and Theoretical Mechanics (ATOM) Laboratory, Department of Mechanical Engineering, Indian Institute of Technology Indore, Simrol, Indore 453 552, India
e-mail: kundalwal@iiti.ac.in

P_x and P_z	Polarizations along the x- and z-direction
q_i	Ion charge of the ith atom
r_i	x-coordinate of the ith atom
N	Number of atoms
A	Surface area
D	Bending stiffness
ΔE	Bending potential energy
θ_{ijk}	Angle between bonds
θ	Angle between two vectors
ε_{xz}	Strain in the x-direction due to deformation in the z-direction
e_{ijk}	Piezoelectric coefficients
μ_{ijkl}	Flexoelectric coefficients

Acronyms

BN	Boron nitride
BNS	Boron nitride nanosheet
BGH	Boron nitride-graphene heterostructure
BCN	Carbon-doped boron nitride nanosheet
MD	Molecular dynamics
DFT	Density functional theory
CVD	Chemical vapor deposition
EBR	Electron beam irradiation

1 Introduction

Nanotechnology has brought the revolutionary age of boron nitride (BN) and carbon-based nanomaterials such as nanotubes [1] and nanosheets [2, 3]. These materials possess excellent physical characteristics that are quite different from their parent materials at the microscale level [4, 5]. The following two-dimensional (2D) nanomaterials attracted a lot of attention in academia and industry: (i) graphene sheets, hexagonal arrays of carbon (C) atoms, and (ii) BN sheets (BNSs), hexagonal arrays of boron (B) and nitrogen (N) atoms [6]. BNSs are often used in various applications such as high temperature environments, solid lubricants, heat sinks and nanoelectromechanical systems (NEMS). In the case of graphene sheets, chemical and thermal stability might be a problem [7]. Furthermore, a BNS possesses a non-centrosymmetric structure, is nonmetallic and has a higher band gap (~5 to 6 eV) [1]. Due to the difference in the electronegativities of the B and N atoms of BNS, it shows a partially ionic characteristic [8], making it a piezoelectric material. Piezoelectricity is a response of electric polarization to a mechanical strain, and it appears only in non-centrosymmetric dielectric crystals.

A BNS with a honeycomb crystal lattice is graphene's sister material, yet it exhibits totally different properties. The BNS is piezoelectric due to a broken sublattice (inversion) symmetry and the degeneracy lifting of the conduction and valence bands at two inequivalent Dirac points [9]. The separation of the centers of the positive and negative charges on the application of in-plane load creates dipole moments in the sheet. The resulting dipole moments produce a polarization and the material shows the flexoelectric effect. Unlike piezoelectricity, the flexoelectric effect is universal and can be found in all dielectrics since the strain gradient breaks the inversion symmetry of the material. Figure 1 shows the piezoelectric effect in a BN unit cell in which arrows indicate the direction of motion of the charges and polarization. Curvature-induced polarization is another way to induce the flexoelectric effect in the monolayer BNS/BGH. As a result of bending of the sheet, a Coulomb repulsion inside a cavity increases with curvature, which leads to a redistribution of the π-orbitals. This results in an electronic charge transfer from the concave to the convex region and induces the normal atomic dipole at each atomic site. Note that there is no dipole moment across the unloaded flat BNS due to the symmetry of the π-orbitals (see Fig. 1d). By bending the sheet, we can introduce asymmetry in the π-orbitals (see Fig. 1e). Therefore, Coulomb repulsion inside the cavity increases with curvature and leads to a redistribution (rehybridization) of the π-orbitals from sp^2 to something inbetween sp^2 and sp^3. Figure 1e demonstrates that the boron (B) and nitrogen (N) atoms in the bent BNS are not in the tangential plane, and the three σ_i-bonds ($i = 1,\ 2,\ 3$) are tilted down with respect to that tangential plane. Redistribution of ions and charges occur upon bending of the BNS, resulting in the formation of a net dipole moment across

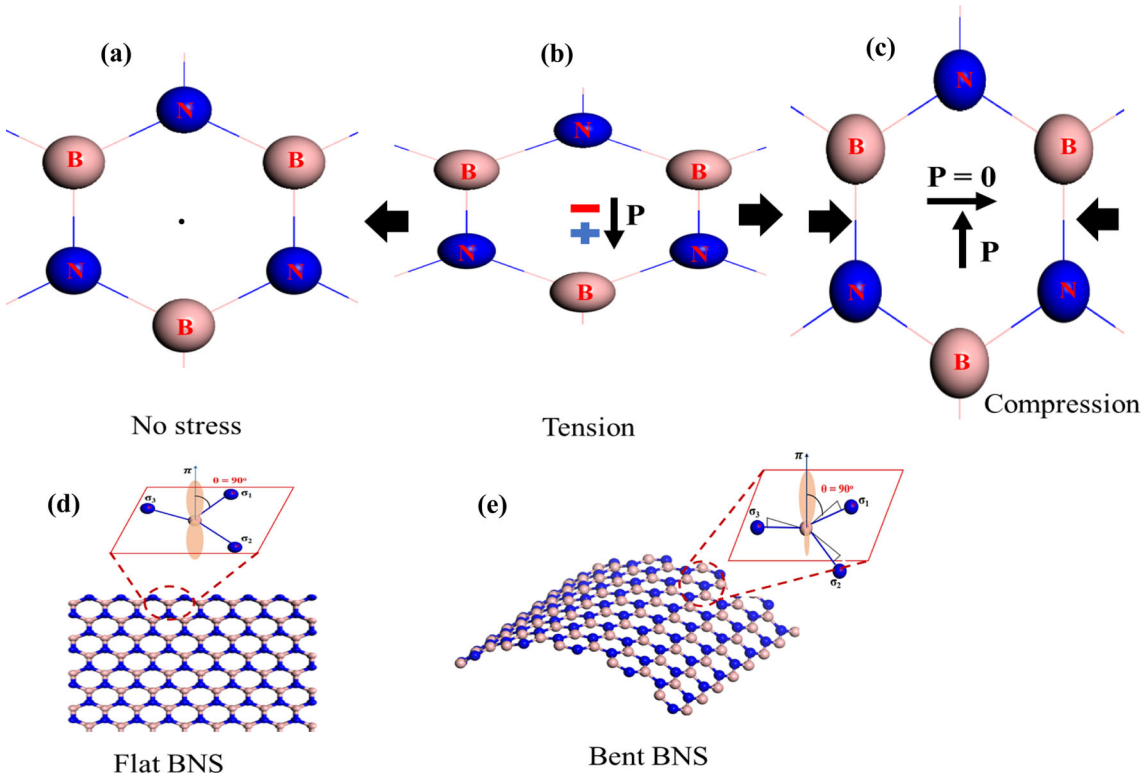

Fig. 1 **a** Stress-free BN lattice, **b** BN lattice under tension, **c** BN lattice under compression, **d** symmetric π-orbitals in planer BNS, and **e** asymmetric π-orbitals in bent BNS

the BNS. The resulting dipole moments produce a polarization, and the BNS shows the flexoelectric effect. The electromechanical response of a BNS is better than the polymer-based piezoelectric materials [8]. BNSs become promising candidates for nanotechnological applications under extreme environmental conditions and for use as reinforcing fillers in advanced nanocomposite structures with desired properties for specific applications. Although these applications are similar to graphene [10, 11], a close analogue of BNS, the latter shows piezoelectricity.

Several unique techniques are being employed to synthesize BNSs, including the chemically derived route technique [12], micromechanical cleavage technique [4], electron beam irradiation (EBR) [13], chemical vapor deposition (CVD) [14] and thermal decomposition of borazine on the surface of a transition metal [15]. From these synthesizing techniques, EBR promotes topological pores/defects such as atom vacancies [13], Stone–Wales [16] and anti-sites doping [17]. Sometimes these pores/defects improve local changes in the atomic polarization and chemical bond orders of a BNS, leading to a change in its electromechanical behavior [18]. Using an energetic EBR technique, a monolayer BNS was successfully synthesized by Jin et al. [13]. They found the existence of B and N monovacancies and triangular pores in BNSs. Using an atomic force microscope, a bending test was performed by Li et al. [7] to investigate the bending modulus of BNSs with a thickness of 25–300 nm and sizes of 1.2–3.0 μm. They found that the bending moduli of BNSs decrease with their thickness. Guo et al. [19] synthesized high-quality BNS thin films with controllable thickness by low-pressure CVD method. They observed that a thin film of BNS has a higher band gap of ~ 5.57 eV and high breakdown strength of ~ 9.0 MV/cm. Therefore, it can be used as the dielectric in curved capacitors. Pioneering experiments of different 2D nanomaterials by Wu et al., [20] confirmed that the piezoelectric effect is induced by stretching and releasing of single layer (SL) molybdenum disulfide (MoS_2). They reported that an odd number of stacked layers shows the piezoelectric effect, while there is no piezoelectric effect observed in the even number of stacked layers. Brennan et al. [21] theoretically predicted and experimentally confirmed that MoS_2 SL exhibits out-of-plane electromechanical coupling, which is attributed to the flexoelectric effect. It is challenging to isolate the relative contributions of piezo- and flexoelectricity stemming from the resulting polarization to calculate the flexoelectric coefficients of 2D nanomaterials.

The piezo- and flexoelectricity phenomena were intensely studied experimentally and theoretically in the literature [22, 23]. A BNS shows extraordinary dielectric properties with a stunning and homogeneous performance for its nanodevice applications [9]. Besides, high piezoelectricity is observed in BNSs [24, 25]. These exceptional properties of BNSs provide new opportunities for developing novel piezoelectric devices [26]. Using first-principle calculations, Dumitirica et al. [27] determined the normal polarization induced by bending of graphene shells, which microscopically occurred due to a shift in sp^2 hybridization at each atomic site. During bending deformation, the center of electronic charge is displaced outwards from the nuclear charge, and at the corresponding curvature, induced dipole moments were observed. Kalinin and Meunier [28] applied density functional theory (DFT) to study the flexoelectric effect in 2D nanomaterials. They observed that a induced dipole moment and bending curvature of the graphene sheet show a linear relationship. Duerloo et al. [29] performed DFT to examine the electromechanical coupling in the few layers of BNS. This study reveals that BN bilayer exhibits a strong mechanical coupling between curvature and electric fields. A theoretical study performed by Kvashnin et al. [30] on the flexoelectric effect in carbon-based nanostructures such as nanocones, fullerenes and nanotubes confirmed that the flexoelectric atomic dipole moments depend on the local curvature of the structure. Chatzopoulos et al. [31] analyzed the flexoelectricity in a periclase sample (cubic ionic MgO) using molecular dynamics (MD) simulations. They studied three flexoelectric coefficients using three different inhomogeneous deformation modes. They found that the induced polarization depends linearly on the strength of the strain gradient as well as the primary polarization, which is caused by the displacement of the ionic charges. Kundalwal et al. [32] performed DFT calculations to study the electromechanical response of a graphene sheet containing a non-centrosymmetric pore under uniaxial loading and bending. Using MD simulations, Zhuang et al. [33] developed a charge-dipole potential model to determine the flexoelectric response of 2D nanomaterials such as BNS, MoS_2 and graphene sheets subjected to bending deformation. They prescribed a bending deformation method to calculate the flexoelectric constants while eliminating the piezoelectric contribution from the universal relation of induced polarization during the deformation. They also reported that the electromechanical coupling increases in the case of out-of-plane bending as compared to in-plane stretching. Strain-engineering pathways were also used in the literature to tune the electronic properties of nanostructures [34–37]. For instance, Barani et al. [34] showed that a wide gap in the phonon DOS can be created in a BN structure by applying 20% elastic strain in the zigzag direction. Similarly, Baimova [35] found that the physical properties of graphene can be controlled by means of strain engineering.

Wang et al. [38] developed an analytical approach to study the field-induced alignment of cantilevered graphene nanoribbons. They revealed that the bending angle of graphene is approximately proportional to the square of the field strength and the graphene sheet's length, while it does not depend on the width of the graphene sheet. Scarpa et al. [39] investigated the out-of-plane bending behavior of SL graphene sheets using an atomistic continuum model. They found that the bending stiffness of graphene sheets depends on the bending curvature. Ma et al. [40] used the molecular mechanics model to determine the bending properties of SL graphene sheets. They reported that the bending stiffness of graphene sheets significantly depends on the chiral angle and chirality of the nanostructures, especially when the bending curvature is large. Using classical MD simulations, Thomas et al. [41] determined the mechanical properties of BNSs. They found that Young's modulus and Poisson's ratio are anisotropic for finite sheets, whereas they are isotropic for the infinite sheet. They also calculated the bending rigidity of BNS systems subjected to in-plane bending and out-of-plane stretching modes using the Foppl–von Karman approach. González et al. [42] performed the bending deformation of 2D nanostructures such as graphene sheet, MoS_2 and imogolite using MD simulations. They reported that the edge effects of a thin graphene sheet can significantly decrease its bending modulus.

Doping is the most effective method to enhance material properties such as electronic, thermal, optical, magnetic and chemical properties [43–45]. Several experimental and theoretical studies found that C atoms can be easily doped into the BN-based nanostructures [46, 47] in view of harmony with neighboring B and N atoms. Such C-doped BNS can be used in various applications. For instance, Terrones et al. [6] synthesized C-doped nanotubes and nanosheets. They found enhancements in the electronic and structural properties of C-doped BN-based nanomaterials. Bhattacharya et al. [48] studied the electronic properties of functionalized BNSs with various functional groups such as H, F, OH, CN, NH_2 and CH_3, using first-principles calculations. DFT calculations were performed by Gao et al. [49] to analyze the catalytic activation and the adsorption of C-doped BNS. Using MD simulations, Zhang et al. [50] examined the thermal conductivity of various 2D nanomaterials such as graphene sheets, BNSs and BCN. They reported higher thermal conductivity for BCN compared to graphene sheets and BNS. Beniwal et al. [51] performed experimental and theoretical investigations of graphene-like 2D nanomaterials composed of B, C and N atoms. Using first-principles calculations, they found that the electronic band gap of BCN is 1.5 eV and this value lies between the band gap value of the

gapless graphene sheet and the insulating BNS. Thomas and Lee [52] studied graphene, BN and BCN sheets using MD simulations and described their anisotropic electrical, mechanical, thermal and optical properties.

BN and graphene-based nanostructures are ideal reinforcements for nanocomposite structures because of their high strength and stiffness as well as low mass density [53–55]. For instance, Yan et al. [56] studied the thermal and mechanical properties of hybrid BNS and BNNT-based epoxy nanocomposites. They found that the epoxy/BNSs-BNNTs are homogeneously dispersed in BNSs–BNNTs and provide strong filler–matrix interface interaction. They also show that the thermal conductivity and Young's modulus are increased by 95% and 57% by adding only a 1% volume fraction of BNSs–BNNTs.

Heterostructures are often expected to provide better electronic properties than homogeneous structures. The ability to control the formation of interfaces between different monolayers has become one of the foundations of modern materials science. With the advent of 2D crystals, low-dimensional equivalents of conventional interfaces can be envisioned: triangular, trapezoidal and circular boundaries separating different materials integrated in a single 2D heterostructure [57].

The literature review reveals that few investigations exist on BNSs under in-plane and out-of-plane loads to study their electromechanical response. To the best of the authors' knowledge, no study has reported the out-of-plane polarization and flexoelectric effect in monolayer boron nitride-graphene heterostructures (BGHs). This has inspired us to conduct this study to determine the electromechanical response of BGHs with different shapes of graphene domains: triangular, trapezoidal and circular. The out-of-plane polarization and bending stiffness of BGHs under uniaxial and bending deformations were calculated using MD simulations. In the present study, the armchair type of BNSs was considered.

2 Computational modelling of BNS/BGHs

MD simulations were performed in the current study to study the electromechanical response of pristine BNS and BGHs. All MD simulations were performed using open source software, LAMMPS [58], and visualization is performed using OVITO visualization software [59]. It is well known that for MD simulations of BGH systems, it is crucial to accurately describe the interatomic interactions between B, C and N atoms. The Tersoff potential [60] has been successfully employed in previous studies to determine the mechanical, piezoelectric and flexoelectric properties of BN-based nanomaterials [61]. Therefore, the interatomic interactions between B, C and N atoms were described using the three-body Tersoff potential force field [60]. The total energy (E) of the atomic structure is a function of the distance between two neighboring atoms i and j, as follows [3, 62, 63]:

$$E = \sum_i E_i = \frac{1}{2} \sum_{i \neq j} V_{ij}, \tag{1}$$

$$V_{ij} = f_C(r_{ij}) \left[f_R(r_{ij}) + b_{ij} f_A(r_{ij}) \right], \tag{2}$$

where E is the total energy of the system, E_i is the site energy, and V_{ij} is the bond energy. The indices i and j run over the atoms of the system. The term r_{ij} is the distance between atom i and j, while b_{ij} is the bond angle term which depends on the local coordination of atoms around atom i. The terms f_R and f_A are the repulsive and attractive pair potentials, respectively.

The term f_C is the cut-off function provided to limit the potential range and thus saves the computational resources required in MD simulations.

The pair-like attractive and repulsive energies are given as follows:

$$V_{ij}^R = f_C(r_{ij}) f_R(r_{ij}), \tag{3}$$

$$V_{ij}^A = f_C(r_{ij}) b_{ij} f_A(r_{ij}), \tag{4}$$

and the cut-off function $f_C(r)$ is defined as:

$$f_C(r_{ij}) = \begin{cases} 1 & r_{ij} < R_{ij}, \\ \frac{1}{2} + \frac{1}{2} \cos\left(\pi \dfrac{r_{ij} - R_{ij}}{S_{ij} - R_{ij}} \right) & R_{ij} < r_{ij} < S_{ij}, \\ 0 & r_{ij} > R_{ij}, \end{cases} \tag{5}$$

where R and D are model specific parameters. The two-body repulsion term $f_R(r_{ij})$ and attraction term $f_A(r_{ij})$ are given by:

$$f_R(r_{ij}) = -A_{ij}\ \exp\left(-\lambda_{ij}^{I} r_{ij}\right), \tag{6}$$

$$f_A(r_{ij}) = -B_{ij}\ \exp\left(-\lambda_{ij}^{II} r_{ij}\right), \tag{7}$$

where A_{ij} , B_{ij} , λ_{ij}^{I} and λ_{ij}^{II} are model specific parameters. The three-body interactions are given by b_{ij}:

$$b_{ij} = \left(1 + \beta^n \zeta_{ij}^n\right)^{-\frac{1}{2n}}, \tag{8}$$

$$\zeta_{ij} = \sum_{k\neq i,\ j} f_c(r_{ijk}) g(\theta_{ijk}) \exp\left[\lambda_3^m (r_{ij} - r_{ik})^m\right], \tag{9}$$

where β, λ_3, m and n are model specific parameters. The term θ_{ijk} denotes the angle between bonds ij and ik. The angular dependent term $g(\theta)$ is given as

$$g(\theta) = \gamma_{ijk}\left(1 + \frac{c^2}{d^2} - \frac{c^2}{d^2 + (\cos\theta - \cos\theta_0)^2}\right), \tag{10}$$

where θ is the angle between two vectors r_{ij} and r_{ik}; and γ_{ijk}, c, d and θ_0 are model specific parameters [64].

First, preliminary structures of BNSs were created with a bond length of 1.446 Å [65]. Then, the primary structures of BNSs were optimized by minimizing their energy using the conjugate gradient method. The structure was treated as optimized when the difference in its total potential energy between two consequent steps was less than 1.0×10^{-10} kcal/mol [66–69]. The NVT ensemble was used to update velocities and positions of B and N atoms after each time step of 0.5 fs using the Nosé-Hoover thermostat [70]. NVT is the constant number of atoms, temperature and volume ensemble, and during the simulation, it allows to maintain the constant temperature by scaling the velocities of atoms in a fixed volume. The simulations were performed with a periodic boundary conditions in all directions of the sheet, and the simulation box was kept large enough to avoid the interlayer interactions. To perform the bending deformation, a BNS/BGH sheet was divided into vertical rectangular bins. For bending deformation, a strain gradient was applied on each vertical rectangular bin for a period of 1 ps, following a relaxation of 50 ps for the equilibration. At each vertical rectangular bin, deformation gradually increases from the left to the middle section of the sheet, and maximum deformation occurs in the middle portion of the vertical rectangular bins. The bending deformation mainly depends on the bending curvature (non-uniform strain gradient on each bin). The standard velocity Verlet algorithm was used to integrate Newton's equations of motions [71]. The flat BNS was bent along the z-direction, while both left and right edges were fixed. The schematic representation of the flat and bent configurations of BNS is shown in Figs. 2a and b.

2.1 Curve fitting

The present study deals with the bending deformation of BNS/BGH from which we can directly calculate flexoelectric coefficients by eliminating the piezoelectric terms from the overall polarization. The radius of curvature, R, is used to analyze the bending deformation of BNS/BGH. The term k denotes the strain gradient/bending curvature, which is the inverse of the radius of curvature R. Figure 2b depicts the curve fitting of a bending configuration of BNS when the curvature radius is 111.11 Å. The strain and strain gradient curves can be calculated from the displacement fitting relations described by Tan et al. [72].

The bending displacement of a point in BNS/BGH may be expressed as follows:

$$S_z(x) = -px^2 + q, \tag{11}$$

where p and q denote the parameters of curve fitting which can be calculated from the following relations:

$$\frac{1}{R} = k = \left|\frac{\partial^2 S_z(x)}{\partial x^2}\right| = -2p\ , \tag{12}$$

$$S_z(x_{\max}) = -px_{\max}^2 + q\ = 0. \tag{13}$$

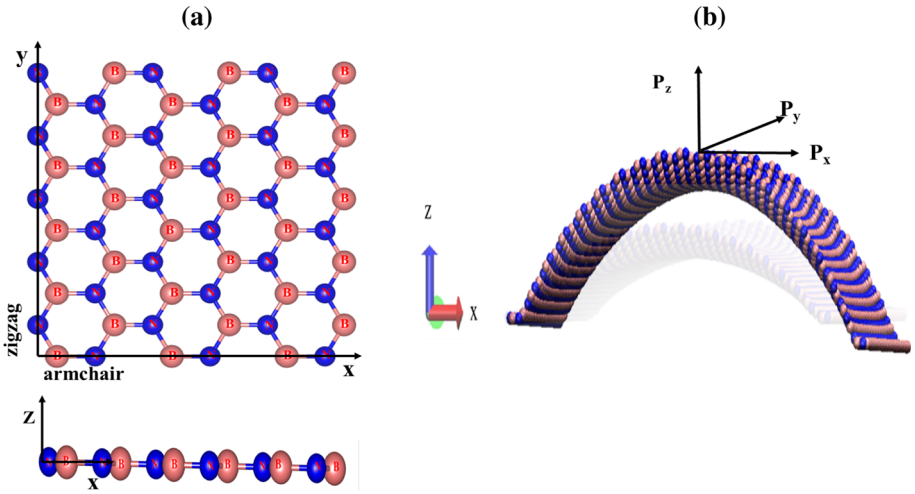

Fig. 2 Schematic representations of **a** flat **b** bent BNSs

Using Eqs. (11–13), we can obtain the value of $p = \frac{k}{2}$ and $q = \frac{k}{2}x_{max}^2$, where x_{max} is half of the length L_x of BNS/BGH along the direction of x.

The strain components, ε_{xz}, can be calculated as follows:

$$\varepsilon_{xz} = \frac{1}{2}\frac{\partial S_z\,(x)}{\partial x} = -\frac{k}{2}x. \tag{14}$$

It is important to note that the displacements of atoms during bending deformation are along the principal curvature direction and we can get a unique solution of atomic displacement along the z-axis $S_z(x) = 0$, and therefore, $\varepsilon_{xz} = 0$. As the strain depends on both k and x, a larger strain is obtained by enlarging the radius of curvature or the length of 2D nanomaterial along the x-axis.

Strain gradients depend on the curvature of sheets. In the present case, only the nonvanishing strain gradient component is constant and can be expressed as:

$$\frac{\partial \varepsilon_{xz}}{\partial x} = \left|-\frac{k}{2}\right|. \tag{15}$$

The dipole moment induced due to the redistribution of atomic charges under the bending deformation and the resulting polarization can be calculated using the following relation [72]:

$$P = \sum_{i}^{N} \frac{q_i r_i}{A}, \tag{16}$$

where q_i denotes the ionic charge of the ith atom, r_i is the x-coordinate of the ith atom, N is the number of atoms, and A is the flat sheet area [72]. Equation (16) was used to calculate the induced polarization along the x- and z-directions of BNSs/BGHs. From the modern theory of atomic polarization, the value and direction of total polarization represent the vector sum of all elementary dipole moments per unit area of BNS [73]. To determine the normal polarization, the vertical rectangular bins are cut into several parts along the x- and y-axes to calculate normal polarization distribution.

Flexoelectricity can be found in all insulators; therefore, the polarization can be induced by applying inhomogeneous deformation. The flexoelectricity is a coupling between polarization and strain gradient, while piezoelectricity is a coupling between the polarization and homogeneous strain. The constitutive relation for the polarization vector induced due to the flexo- and piezoelectricity effects may be written as:

$$P_i = e_{ijk}\varepsilon_{jk} + \mu_{ijkl}\frac{\partial \varepsilon_{jk}}{\partial x_l}, \tag{17}$$

where e_{ijk} and μ_{ijkl} are the respective piezoelectric and flexoelectric tensors; ε_{jk} and $\frac{\partial \varepsilon_{jk}}{\partial x_l}$ are the strain and strain gradient, respectively.

Substituting Eq. (15) into Eq. (17) and assuming that the imposed mechanical deformation in Eq. (11) removes the piezoelectric contribution, we can obtain

$$P_i = \mu_{ijkl} \frac{\partial \varepsilon_{jk}}{\partial x_l}, \tag{18}$$

$$P_z = \mu_{zxzx} \frac{k}{2}, \tag{19}$$

where μ_{zxzx} is the out-of-plane or bending flexoelectric coefficient and P_z represents the out-of-plane polarization. A closer look raises an important question regarding the in-plane and out-of-plane polarization. To generate the out-of-plane flexoelectric constants, the mechanical bending imposed to sheet deforms the sheet in the z-direction, and due to that, polarization is induced in the z-direction that is called out-of-plane-polarization (P_z). The mechanical bending imposed only generates a constant strain in the x-direction due to applied deformation in the z-direction. The stress in x-direction leads to generate a polarization (P_x) in the x-direction called in-plane polarization. The in-plane polarization P_y in the y-direction is less than the in-plane polarization P_x at a particular bin because significantly less deformation occurs in the y-direction during bending.

2.2 Bending stiffness of BNS

Based on the continuum-mechanics approach, the bending stiffness (D) of BNS/BGH can be determined from the bending potential energy (ΔE) using the following relation [74]:

$$\Delta E = \frac{1}{2} A D R^{-2} = \frac{1}{2} A D k^2, \tag{20}$$

where A is the surface area of BNS/BGH under bending deformation, k is the bending curvature and R is the radius of curvature.

3 Results and discussion

MD simulations were performed to determine the electromechanical response of armchair BNS subjected to out-of-plane deformation. A fixed size of 80 Å × 80 Å of BNS was considered for simulations. A schematic representation of flat and bent armchair BNSs is shown in Fig. 2, respectively. A bending curvature range is considered from 0.001 to 0.009 $Å^{-1}$. First, the MD simulations were performed on the pristine BNS to determine the electromechanical response for different bending curvatures. Further calculations were performed on different BGHs to determine induced polarizations, flexoelectric coefficients (along the x and z-direction) and bending stiffness.

We first considered bending scheme that eliminates the contribution of piezoelectric effect from the total polarization to calculate the intrinsic flexoelectric coefficients. We obtained the strain (ε_{xz}) and strain gradient $\left(\frac{\partial \varepsilon_{xz}}{\partial x}\right)$ in the xz-direction by solving the curve fitting equation (11). During bending deformation, the local atomic strain for each atom i can be calculated using the local deformation gradient F, and it depends on the initial and final coordinates of atoms. The local atomic strain tensor for atom i is as follows:

$$\varepsilon_i = \frac{1}{2}\left[(F_i)^T F_i - I\right], \tag{21}$$

where the term F_i represents the strain gradient, which provides the initial and final deformed coordinates of atoms, and a term I represents the identity matrix. We performed bending deformation of BNS at a bending curvature of 0.001 $Å^{-1}$ by following the simulation procedure described in Sect. 2.1. The values of strain (ε_{xz}) and strain gradient (k) were obtained using curve fitting (Fig. 3a). Figures 3b and c demonstrate the variation of strain (ε_{xz}) and strain gradient (k) with the x-axis position of the BNS. The variation of strain in x-direction of the BNS during deformation is shown in Fig. 3d which is obtained using Eq. (21). To solve the curve fitting equation (11), a parabolic fitting curve can be obtained from the bending displacement of atomic system, as shown in Fig. 3a. This fitting curve mainly depends on the bending deformation that leads to the induced the polarization, which was also described in previous studies for dichalcogenides, silicene, and MoS_2 [33, 75]. The strain was obtained by dividing the atomic system of BNS into several bins of equal width, and the average strain of each bin was recorded. The obtained value of strain is plotted in Fig. 3b, and it can be observed that

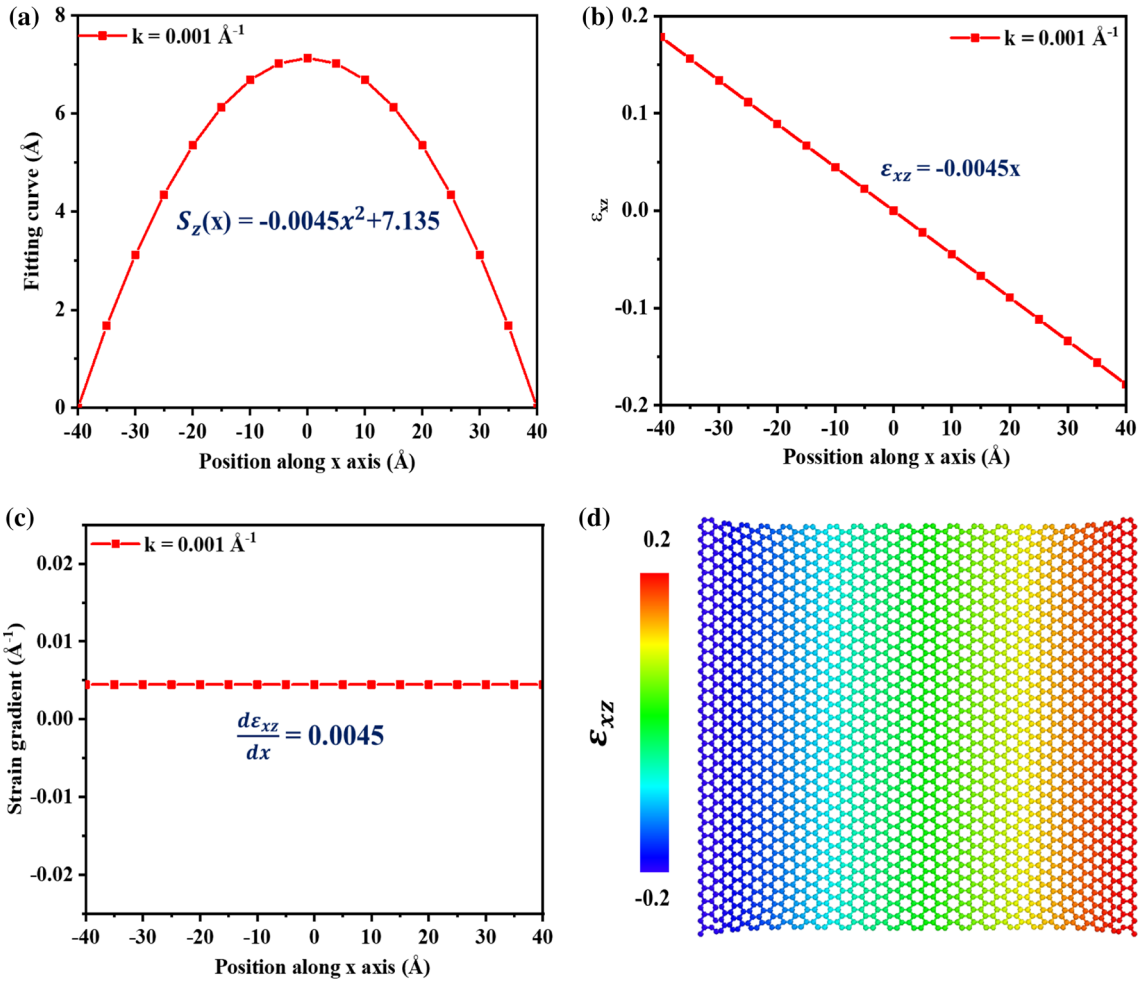

Fig. 3 **a** Curve fitting, **b** strain (ε_{xz}), **c** strain gradient (k) and **d** colored atomic configuration of induced atomic strain in the direction of x of BNS at a bending curvature of 0.001 Å^{-1}

the strain (ε_{xz}) varies linearly along the x direction from − 0.2 to 0.2 of the BNS. A linear negative variation of (ε_{xz}) was observed, which follows the curve fitting equation (14). It can be observed from Fig. 3b that the induced deformation is symmetric, and the resultant in-plane polarization due to strain is canceled out. Hence, the total strain (ε_{xz}) is almost zero (overall summation of the strain of each bin), which removes the contribution of the piezoelectric effect from the polarization in Eq. (17) and satisfies the assumption considered in obtaining Eq. (19). Therefore, during bending deformation, the out-of-plane polarization completely depends only on the strain gradient $\left(\frac{\partial \varepsilon_{xz}}{\partial x}\right)$. The strain gradient $\left(\frac{\partial \varepsilon_{xz}}{\partial x}\right)$ varies along the direction of x plotted in Fig. 3c. The obtained value of the strain gradient along the xz-direction is constant at each time step.

Variation of induced polarizations along the x- and z-directions of the BNS at bending curvatures of 0.006 Å^{-1} and 0.001 Å^{-1} are plotted in Fig. 4. Due to the difference in the electronegativities of the B and N atoms, a net dipole moment is induced, and it is the summation of each dipole moment. We consider respective charges of B, N and C atoms as + 3 eV, − 3 eV and + 2.5 eV with the multiplication of deformed coordinates of atoms along the x- and z-directions of BNS (at each time step). In Fig. 4, green and yellow arrows show the direction and amplitude of polarization which mainly depend on the bending curvature. It can be observed from Fig. 4 that the magnitude of polarization along the z-direction is much higher than along the x-direction. During bending deformation, the magnitude of the induced polarization along the y-direction is negligible; therefore, it is not considered. The previous studies also reported that the curvature-induced charge distribution is present in 2D nanomaterials such as graphene sheet, graphene nanoribbons, BNS and MoS_2 [9, 32, 72]. The mechanical bending was imposed to generate both out-of-plane and in-plane polarizations along the x- and

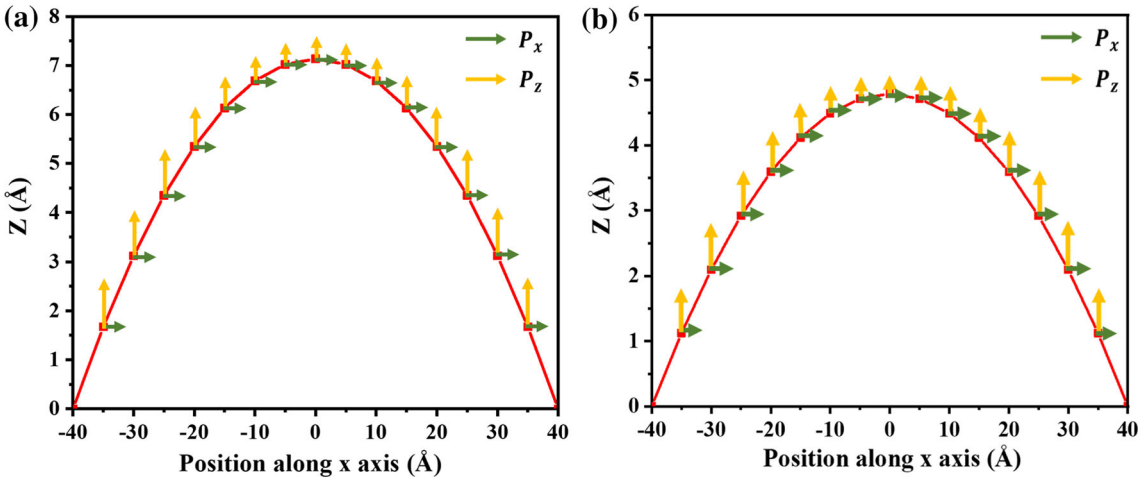

Fig. 4 Variation of induced polarizations along x- and z-directions of BNS at bending curvatures of **a** 0.006 Å^{-1} and **b** 0.001 Å^{-1}

Table 1 Flexoelectric coefficients of pristine BNS and BGHs

Properties		Pristine BNS	BGHs		
			Triangular Triangular	Trapezoidal	Circular
μ_{zxzx} (pC/m)	Present	0.255	0.309	0.289	0.201
	Ref	0.26 [33]	–	–	–

z-directions of BNS. During bending, a strain gradient was induced along the z-direction of the BNS which eventually generates out-of-plane polarization.

The term "flexoelectricity" defines the two-way linear coupling between the electric polarization and the strain gradient [76]. In the case of 2D nanomaterials, bending is the easiest form of deformation to determine a mechanical strain gradient. Upon bending of polar (BNS) materials, the symmetry of the electron distribution breaks in the out-of-plane direction, and a resultant dipole moment is generated at an N atomic site [23]. It can be observed from Fig. 5 that the polarization (P_z) depends on the bending curvature k (strain gradient). The flexoelectric coefficient was calculated from Eq. (18), and the slope of polarization and strain gradient provides the flexoelectric coefficients (μ_{zxzx}) along the principal curvature direction. It can also be observed from Fig. 5 that the out-of-plane polarization using MD simulations fitted suitably into the polarization using the curve fitting technique. The flexoelectric coefficients of pristine BNS reported by numerous researchers using different techniques and the present results are summarized in Table 1. The value of the flexoelectric coefficient of pristine BNS is 0.255 pC/m and shows excellent agreement with the value of 0.260 pC/m obtained by Zhuang et al., [33] using a C-D potential model. Snapshots of bending deformation at bending curvature 0.001 Å^{-1} of pristine BNS with side, top and ortho views are illustrated in Fig. 6. It can be observed from Fig. 6 that the density of charges appears on each B and N atom during bending and such distribution of charge density is uniform in the overall pristine BNS except at the edges (see Fig. 6). The number of electrons is condensed more around the N atoms than around the B atoms due to the former's higher electronegativity, which leads to the dipole moments in BNS. In the present study, the difference in charge density is calculated by subtracting the superposition of isolated atomic charge densities from the corresponding BNS's total charge density (after deformation at each time step). In previous studies, DFT calculations provided significant in-plane polarization and out-of-plane atomic displacement for a corrugated BNS which mainly depends on shifting of π and σ chemical bonds [33]. The minimal difference in out-of-plane displacements of B and N atoms [77, 78] leads to relatively small out-of-plane dipole moments and also suggests that out-of-plane π–σ interactions are stronger, which makes μ_{xxxx} is higher than μ_{zxzx}. The present calculations of induced polarization and flexoelectric coefficients of pristine BNS are in good agreement with the present results obtained using the state-of-the-art ab initio method [79] and MD simulations [33].

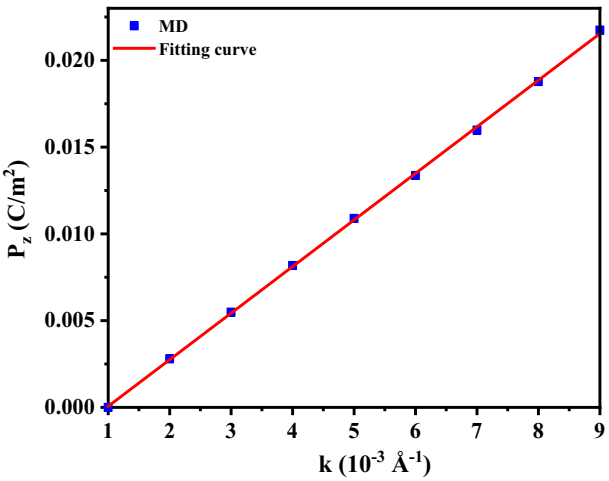

Fig. 5 Variation in polarization (P_z) with strain gradient (k) for pristine BNS

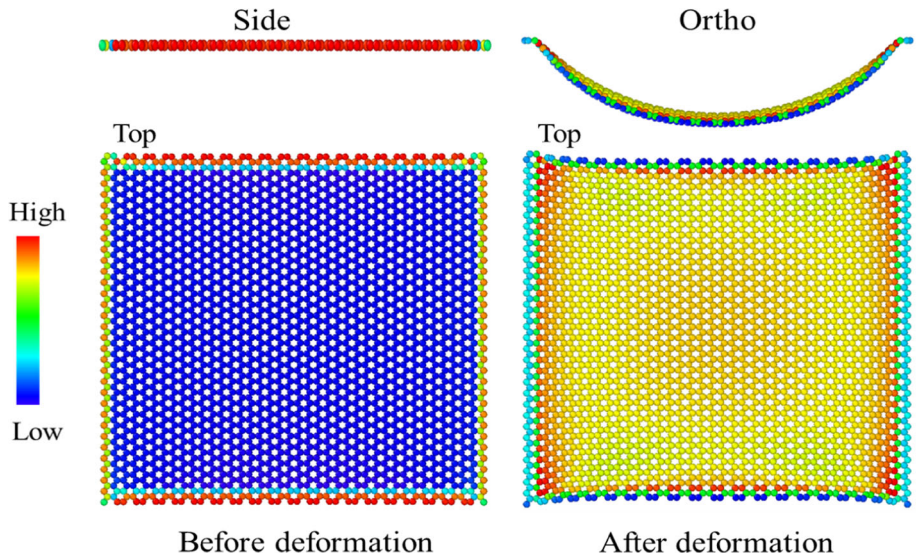

Fig. 6 Snapshots of distribution of charge densities: side, top and ortho views of pristine BNS under bending deformation at bending curvature of 0.001 $Å^{-1}$

3.1 Electromechanical response of BGHs

Interface engineering and dopant engineering allows researchers to modify the mechanical and electronic properties of numerous nanomaterials for specific applications. In the present study, graphene domains are interfaced with BNS in such a way that a non-centrosymmetric interface of graphene-BNS can be created in the resulting monolayer heterostructure (see Fig. 7). All C atoms at the interface are partially covalent with N atoms. Integration of graphene domains with BNS was considered because B, C and N atoms have the same planar sp^2 hybridization [80]. To examine the effect of different graphene domains, four cases of armchair BNSs were considered: pristine, circular graphene domain, triangular graphene domain and trapezoidal graphene domain. Schematic representations of these structures are shown in Fig. 7. Note that a constant C-doping concentration of 5.6% was considered. The doping concentration is the ratio of number of C atoms to the total number of atoms in the sheet.

The explicit simulations were performed with 5.6% concentration of graphene domain [66] irrespective of the shape of the domain. Note that the graphene domain concentration is the ratio of C atoms in BGH to the total number of atoms in pristine BNS. During the in-plane movement, a low polarization occurred in BGH due to the strain gradient at the graphene-BNS interface. However, once BGH is bent, the π-σ

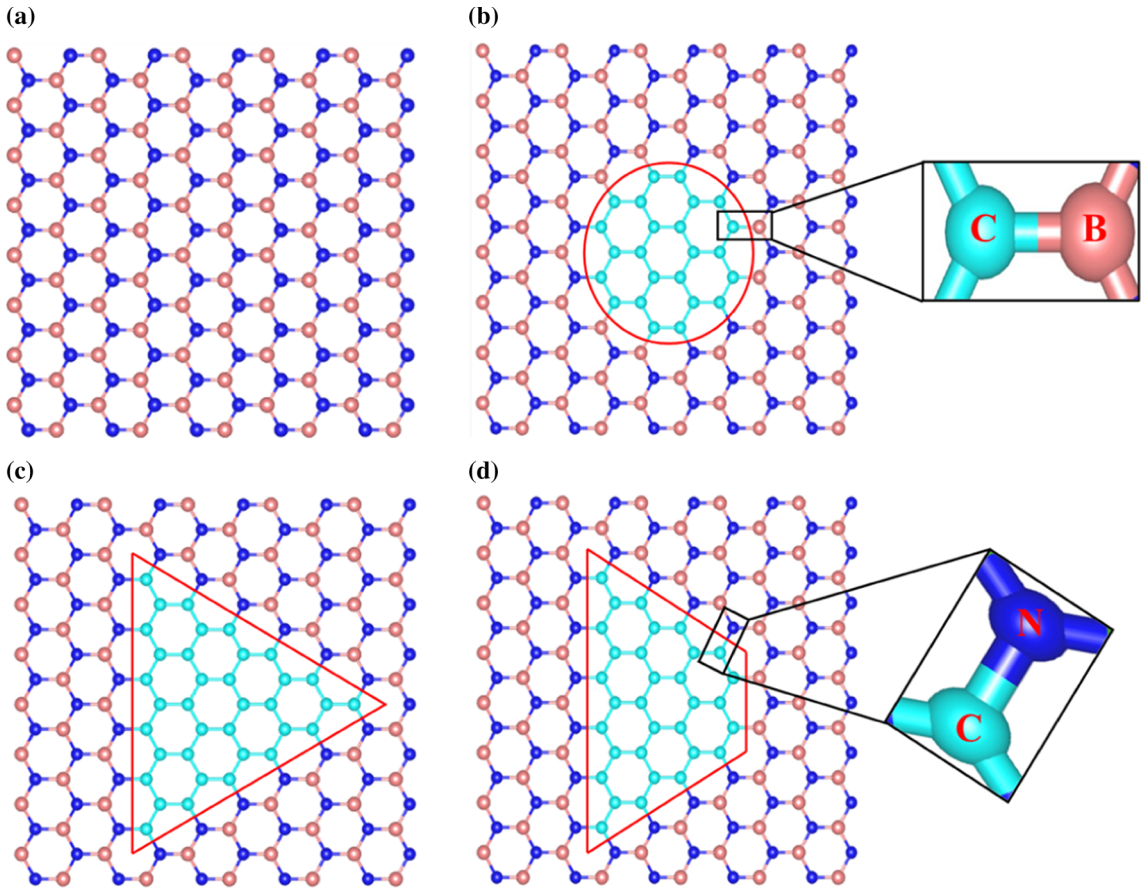

Fig. 7 Schematic representations of **a** pristine BNS, **b** BGH with circular graphene domain, **c** BGH with triangular graphene domain and **d** BGH with trapezoidal graphene domain

interactions begin to increase, which induces a net non-zero dipole moments normal to the sheet. In the out-of-plane displacement, the inversion symmetry of graphene domain breaks due to its bending, leading to π-σ interactions. Therefore, π-σ interactions modify the charge density state of C atoms which induces polarization [27, 32]. It is important to note that during the out-of-plane displacement, planar hybridization of BNS is in between sp^2 and sp^3 hybridization [9]. This results in partial ionic charge transfer from a concave to convex region [32]. This is also in good agreement with the recent studies on graphene sheets and BNSs where the polarization was calculated using DFT [32], MD [33] and ab-initio simulations [32].

Furthermore, the flexoelectric effect of BGH was studied by considering out-of-plane polarization, P_z, plotted as a function of k as shown in Fig. 8. Snapshots of the distribution of charge densities of BGHs (with triangular, trapezoidal and circular graphene domains) for the bending curvature of 0.001 $Å^{-1}$ of BGH are illustrated in Fig. 9. As expected, with increasing k, the induced polarization also increases due to the asymmetry of the π orbitals in C and N atoms. The flexoelectric coefficients of BGHs were obtained from a linear fitting of polarization as a bending curvature function, listed in Table 1. It can be observed from Fig. 8 that the bending of BGHs with triangular and trapezoidal graphene domains provides higher out-of-plane polarization (P_z) due to the breaking of the symmetry of the π orbitals of the C atoms compared to the in-plane polarization (P_x) induced due to the strain-gradient polarization arising from the non-centrosymmetric interface of graphene-BNS domains. It can also be observed that more N atoms in BNS that are partially covalently bonded with C atoms (see Fig. 9) induce more dipole moments due to higher electronegativity differences in the C–N bonds than in the C–B bonds. This leads to higher out-of-plane polarization in BGH (see Fig. 9). It can be observed from Figs. 9a and b that the distribution of charge density of triangular and trapezoidal cases is divided into two parts: (i) uniform in the overall BNS except at the edges and (ii) at C-N covalent bonds. The distribution of charge density in BGH is mostly around the C and N atoms due to higher deformation of C–N bonds and higher electronegativity of N atoms than B atoms (See Figs. 9a and b). It can also be observed from Figs. 9a and b

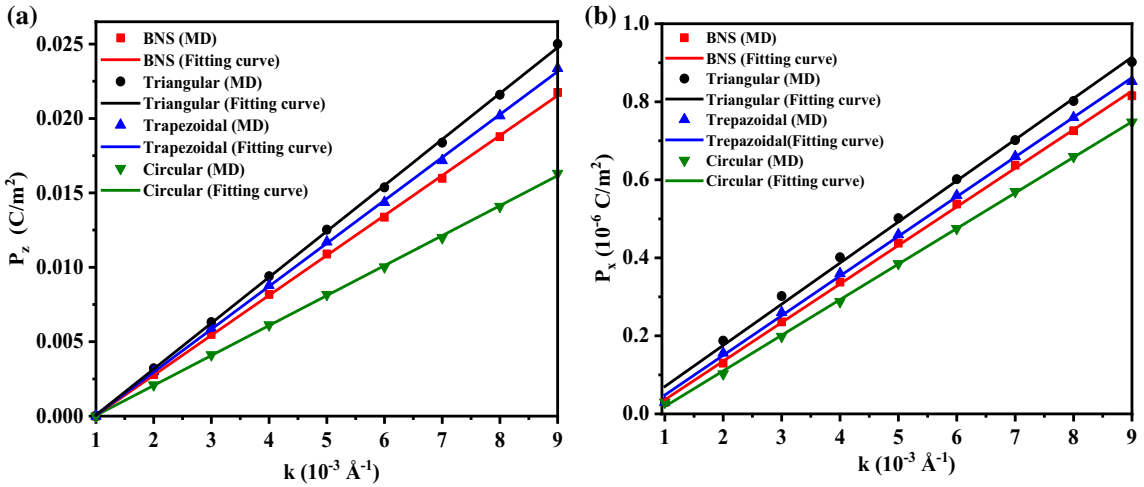

Fig. 8 The variation of **a** polarization in the z-direction (P_z) and **b** polarization in the x-direction (P_x) with strain gradient k for pristine BNS and BGHs

that during out-of-plane displacement, inversion symmetry of C–C atoms breaks which improves the induced dipole moments for the triangular and trapezoidal cases. An enhancement of 15.28% and 7.83% was observed in the value of flexoelectric coefficient (μ_{zxzx}) of BGH with triangular and trapezoidal graphene domains along the z-direction, respectively, while a reduction of 25% was observed for the circular graphene domain in BNS. This is attributed to the fact that the circular graphene domain does not break the symmetry of BGH. Therefore, the induced dipole moments across the circular graphene-BNS interface are found to be symmetric and get canceled out (see Fig. 9c). An enhancement of 2.95% and 2.83% was observed in the flexoelectric coefficients (μ_{xxxx}) of BGH with triangular and trapezoidal graphene domains along the x-direction, respectively, while a reduction of 7.62% was observed for the circular case.

Moreover, we also studied the bond length variation of BGHs at different bending curvatures. The schematic representation of bond length variation (Å) for different BGHs is demonstrated in Fig. 10 at a fixed bending curvature of 0.001 $Å^{-1}$. It is worth noting that the bending modifies the bond length and accordingly, the inversion symmetry of π orbitals of C and N atoms breaks differently (see Fig. 10). In the case of pristine BNS, B–N bond length variation (Å) ranges from 1.446 Å to 1.450 Å, while in the case of BGH, B–N, C–B, C–C, and C–N bond length variations (Å) are 1.446 Å to 1.450 Å, 1.421 Å to 1.436 Å, 1.421 Å to 1.434 Å, and 1.446 Å to 1.463 Å, respectively. This bond length variation mainly depends on the distribution of charges on the B, C and N atoms.

3.2 Bending stiffness of BGHs

In the previous results, the electromechanical response of 80 Å × 80 Å BNS/BGH was studied for a constant 5.6% graphene domain concentration. Further, MD simulations were performed to determine the bending stiffness of BGHs. Figure 2 demonstrates the bending response of BNS/BGH along the principal curvature direction. The variation of potential energy of pristine BNS and BGHs follows a quadratic bending energy relationship between ΔE and k as given by Eq. (20). It can be observed from Fig. 11a that during bending displacement, higher potential energy is stored in the middle portion of the rectangular bins of BNS/BGH because of their higher deformation, and it reduces with the fixed ends of the BNS/BGH (left and right sides of the rectangular bins). It can also be observed from Fig. 11a that the potential energy of triangular, trapezoidal and circular cases increases because covalent C–C bonds of graphene domains show strong π and σ interatomic interactions compared to pristine BNS. Note that B–N bonds of BNS possess weak π and σ interatomic interactions due to the difference of electronegativities of B and N atoms [74, 81]. Therefore, BGH stores higher potential energy compared to pristine BNS at the same strain gradient, which is in good agreement with existing results [82].

The bending stiffness is one of the essential mechanical properties of membranes and layered structures. From previous studies, it was identified that the bending stiffness of SL BNS depends on different parameters

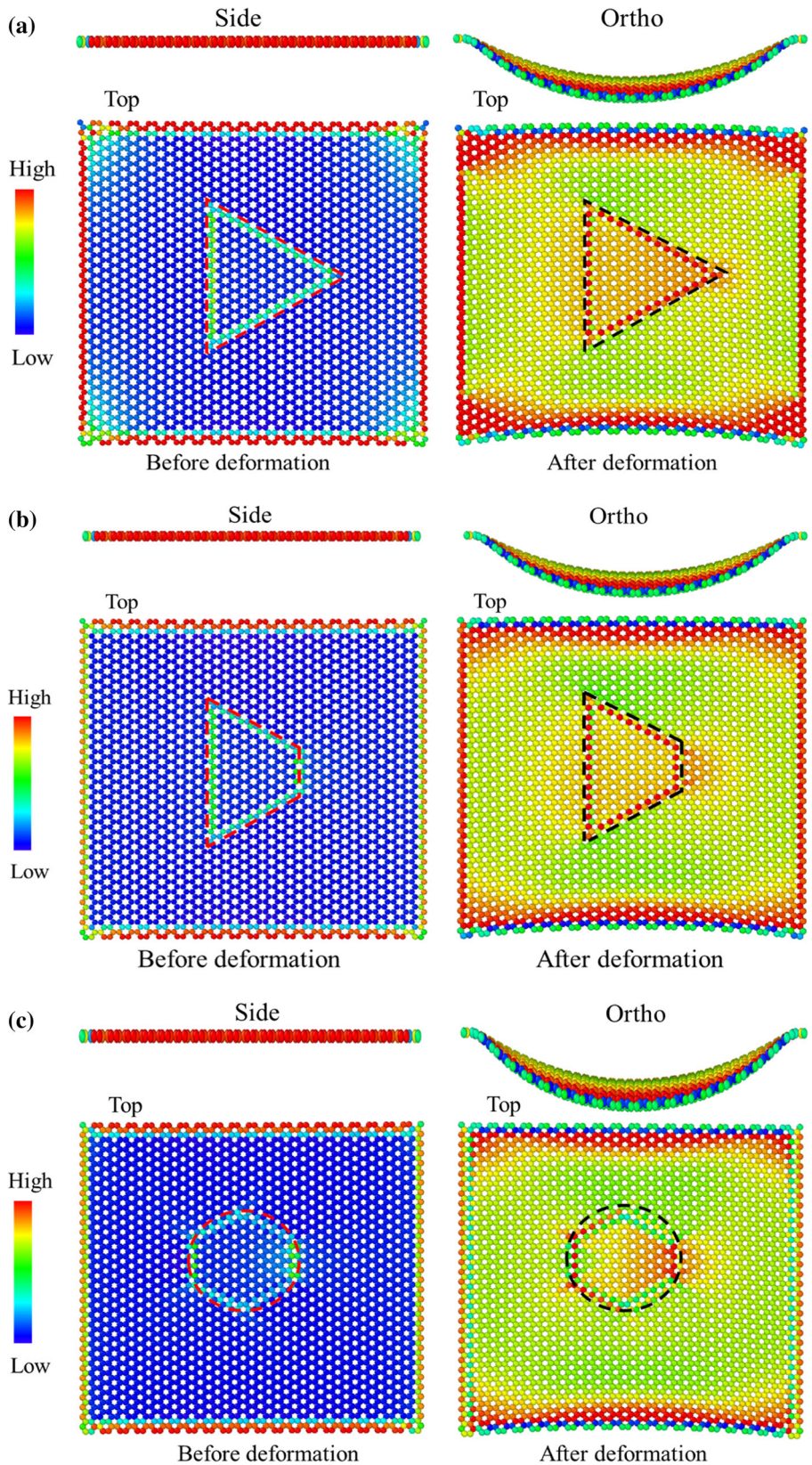

Fig. 9 Snapshots for distribution of charge densities: side, top and ortho views of BGHs with **a** triangular, **b** trapezoidal, and **c** circular graphene domains under bending deformation at bending curvature of 0.001 $Å^{-1}$

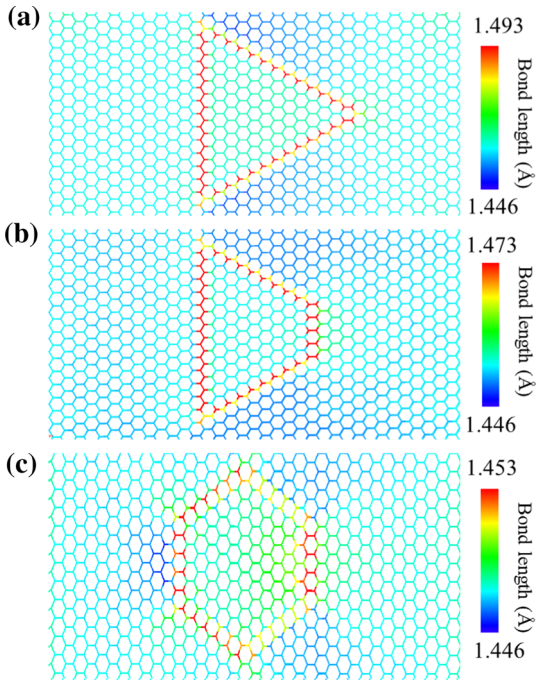

Fig. 10 Schematic representations of variation in bond length (Å) for BGHs with: **a** triangular, **b** trapezoidal and **c** circular graphene domains at bending curvature of 0.001 $Å^{-1}$

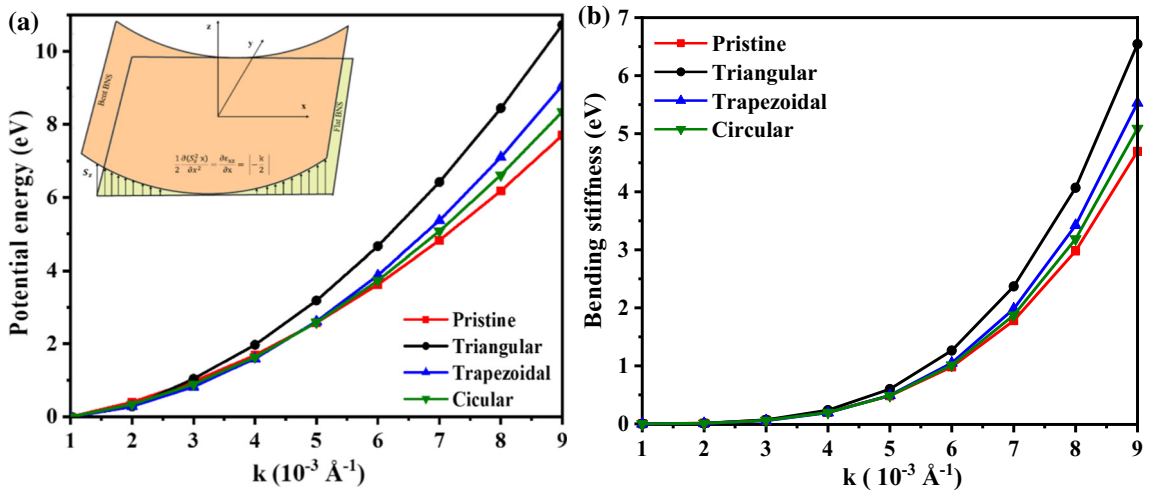

Fig. 11 The variation of **a** potential energy and **b** bending stiffness of BNS and BGHs under different bending curvatures

such as chiral angle, chirality and bending curvature [40]. The bending stiffness of BNS/BGH increases when the bending curvature increases as shown in Fig. 11b. BGHs show higher bending stiffness due to the integration of graphene domains at approximately 1.35–1.68 eV, while partially ionic B–N bonds show less bending stiffness around 1.2–1.4 eV [82, 83] because of electronegativity difference of B and N atoms. Bending stiffness of BNSs reported by numerous researchers using different techniques and approximations was compared with present results, listed in Table 2.

Figure 12 shows the existence of corrugations in bent BNS. Note that some of the investigations [9, 84] reported that the large corrugations in the out-of-plane direction occur due to the weaker B–N atomic bonds. Due to such corrugations, the partial ionic characteristic in the BNS layers increases which leads to an enhancement of magnitude of the hardness of 2D bulk BNS compared to the graphene layers. Therefore, the bending stiffness of SL BNS is smaller as compared to the graphene sheet [39] and the graphene domains

Table 2 Bending stiffness of pristine and C-doped BNS

Properties		Pristine BNS	BGHs		
			Triangular	Trapezoidal	Circular
Bending stiffness (eV)	Present	1.25	1.69	1.42	1.33
	Ref	1.2–1.4 [82, 83]	–	–	–

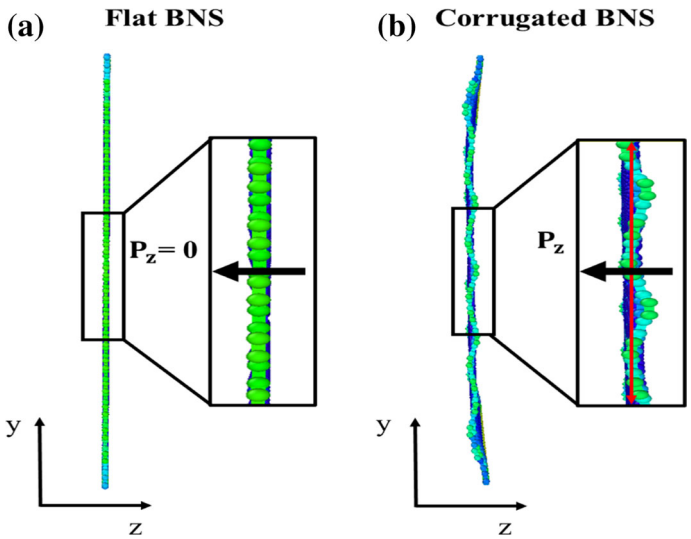

Fig. 12 Side views of **a** flat and **b** corrugated BNSs

can be integrated into the BNS to reduce its hardness. The lowest bending stiffness of 1.25 eV is obtained for pristine BNS due to the partially ionic B–N bonds. The respective bending stiffness of BGH with triangular, trapezoidal and circular graphene domains was observed as follows: 1.69 eV, 1.42 eV and 1.33 eV. The values of bending stiffness of BGH with triangular, trapezoidal and circular graphene domains are enhanced by 35.40%, 13.72% and 6.54%, respectively, along the curvature direction. This observation is also interesting in that curvature-induced anisotropy of BNS must be carefully considered in engineering applications.

4 Conclusions

In the present study, a novel flexoelectric effect in monolayer boron nitride-graphene heterostructures (BGHs) was comprehensively studied using MD simulations with a Tersoff potential force field. Graphene domains with 5.6% of area fraction were interfaced with BNS in different shapes: triangular, trapezoidal and circular. Systematic bending deformations were performed on BNS/BHGs to study the bending stiffness and electromechanical coupling attributed to the piezo- and flexoelectric effects. First, the bending stiffness and flexoelectric coefficients of pristine BNS were compared with previous results and we found good agreement between the present and existing results. The present results reveal that electromechanical coupling of BGHs is enhanced due to the out-of-plane bending compared to in-plane stretching. During bending, the induced atomic polarization along the z-direction of BNS/BGH is higher compared to the x-direction. As bending curvature increases, the induced polarization and bending stiffness of BNS/BGHs are also increased. The flexoelectric coefficients of BGHs with triangular and trapezoidal graphene domains are increased, while the reverse is true in the case of circular graphene domain compared to pristine BNS. A BGH with a triangular graphene domain showed higher polarization than BNS as well as BGH containing other graphene domains. An integration of graphene with N atoms of BNS results in higher dipole moments because the C-N bond is more electronegative than the C-B bond. BGHs with triangular, trapezoidal and circular graphene domains showed higher bending stiffness than pristine BNS. The present work offers a theoretical framework for studying the piezo- and flexoelectric as well as mechanical properties of pristine BNS and monolayer boron nitride-graphene heterostructures.

Acknowledgements The work was fully supported by the Science Engineering Research Board (SERB), Department of Science and Technology, Government of India. S.I.K. acknowledges the support of the SERB Early Career Research Award Grant (ECR/2017/001863) awarded to him.

Availability of data Data available on request from the authors.

Declarations

Conflict of interest The authors declare that they have no known competing financial interests or personal relationships that could have appeared to influence the work reported in this paper.

Appendix A: MD simulations parameters

The parameters n, β, λ_{ij}^{I}, B, λ_{ij}^{II}, and A are used for two-body interactions. The parameters m, γ, λ_3^m, c, d, and $\cos\theta_0$ are used for three-body interactions. R and D are adjustable parameters which can be used for both two- and three-body interactions. The value of $m = 3$, $\beta = 0$, and $\gamma = 1$ are taken as constant. The different parameters λ_{ij}^{I}, λ_{ij}^{II}, A_{ij} , B_{ij} , R_{ij} , and S_{ij} for species i and j can be calculated using the following mixing rules:

$$\lambda_{ij}^{I} = \frac{1}{2}\left(\lambda_i^{I} + \lambda_j^{I}\right), \tag{A1}$$

$$\lambda_{ij}^{II} = \frac{1}{2}\left(\lambda_i^{II} + \lambda_j^{II}\right), \tag{A2}$$

$$A_{ij} = \left(A_i \times A_j\right)^{1/2}, \tag{A3}$$

$$B_{ij} = \left(B_i \times B_j\right)^{1/2}, \tag{A4}$$

$$R_{ij} = \left(R_i \times R_j\right)^{1/2}, \tag{A5}$$

$$S_{ij} = \left(S_i \times S_j\right)^{1/2}. \tag{A6}$$

Refer to Table 3.

Table 3 MD parameters of Tersoff potentials for modeling B-B, N–N, B-N, C–C, C–N and C–B interactions [3, 62, 63]

	B–B	N–N	B–N	C–C	C–N	C–B
m	3	3	3	3	3	3
γ	1	1	1	1	1	1
$\lambda_3^{\mathbf{m}}$	0	0	1.9925	0	0	0
c	0.562	17.795	1092.928	38,049.450	38,049.450	38,049.450
d	0.001	5.948	12.385	4.348	4.348	4.348
$cos\theta_0$	0.500	0.000	− 0.890	− 0.930	− 0.930	− 0.930
h	0.500	0.000	− 0.5413	− 0.930	− 0.930	− 0.930
n	3.992	0.618	0.364	0.727	0.727	0.727
β	0.000	0.000	0.000	0.000	0.000	0.000
λ_{ij}^{II}	2.077	2.627	2.784	2.211	2.205	2.205
B	1173.196	2563.560	3624	430	339.068	387.575
R	2	2	2.3	1.95	1.95	1.95
D	0.1	0.1	0.5	0.15	0.1	0.1
λ_{ij}^{I}	2.237	2.829	2.998	3.487	3.527	3.527
A	1404.052	2978.952	4483.258	1393.635	1386.782	1386.782

References

1. Golberg, D., Bando, Y., Huang, Y., Terao, T., Mitome, M., Tang, C., Zhi, C.: Boron nitride nanotubes and nanosheets. ACS Nano **4**, 2979 (2010)
2. Michel, K.H., Verberck, B.: Theory of elastic and piezoelectric effects in two-dimensional hexagonal boron nitride. Phys. Rev. B Condens. Matter Mater. Phys. **80**, 224301 (2009)
3. Albe, K., Möller, W., Heinig, K.H.: Computer simulation and boron nitride. Radiat. Eff. Defects Solids. **141**, 85 (1997)
4. PaciÍ, D., Meyer, J.C., Girit, Ç., Zettl, A.: The two-dimensional phase of boron nitride: Few-atomic-layer sheets and suspended membranes. Appl. Phys. Lett. **92**, 133107 (2008)
5. Shah, P.H., Batra, R.C.: Elastic moduli of covalently functionalized single layer graphene sheets. Comput. Mater. Sci. **95**, 637–650 (2014)
6. Terrones, M., Grobert, N., Terrones, H.: Synthetic routes to nanoscale BxCyNz architectures. Carbon N. Y. **40**, 1665–1684 (2002)
7. Li, C., Bando, Y., Zhi, C., Huang, Y., Golberg, D.: Thickness-dependent bending modulus of hexagonal boron nitride nanosheets. Nanotechnology **20**, 385707 (2009)
8. Noor-A-Alam, M., Kim, H.J., Shin, Y.H.: Dipolar polarization and piezoelectricity of a hexagonal boron nitride sheet decorated with hydrogen and fluorine. Phys. Chem. Chem. Phys. **16**, 6575–6582 (2014)
9. Naumov, I., Bratkovsky, A.M., Ranjan, V.: Unusual flexoelectric effect in two-dimensional noncentrosymmetric sp2-bonded crystals. Phys. Rev. Lett. **102**, 217601 (2009)
10. Wang, J., Li, J.J., Weng, G.J., Su, Y.: The effects of temperature and alignment state of nanofillers on the thermal conductivity of both metal and nonmetal based graphene nanocomposites. Acta Mater. **185**, 461–473 (2020)
11. Su, Y., Li, J.J., Weng, G.J.: Theory of thermal conductivity of graphene-polymer nanocomposites with interfacial Kapitza resistance and graphene-graphene contact resistance. Carbon N. Y. **137**, 222–233 (2018)
12. Han, W.Q., Wu, L., Zhu, Y., Watanabe, K., Taniguchi, T.: Structure of chemically derived mono- and few-atomic-layer boron nitride sheets. Appl. Phys. Lett. **93**, 223103 (2008)
13. Jin, C., Lin, F., Suenaga, K., Iijima, S.: Fabrication of a freestanding boron nitride single layer and Its defect assignments. Phys. Rev. Lett. **102**, 195505 (2009)
14. Shi, Y., Hamsen, C., Jia, X., Kim, K.K., Reina, A., Hofmann, M., Hsu, A.L., Zhang, K., Li, H., Juang, Z.Y., Dresselhaus, M.S., Li, L.J., Kong, J.: Synthesis of few-layer hexagonal boron nitride thin film by chemical vapor deposition. Nano Lett. **10**, 4134–4139 (2010)
15. Lin, Y., Connell, J.W.: Advances in 2D boron nitride nanostructures: nanosheets, nanoribbons, nanomeshes, and hybrids with graphene. Nanoscale **4**, 6908 (2012)
16. Lin, Y., Williams, T.V., Cao, W., Elsayed-Ali, H.E., Connell, J.W.: Defect functionalization of hexagonal boron nitride nanosheets. J. Phys. Chem. C. **114**, 17434–17439 (2010)
17. Weng, Q., Wang, X., Wang, X., Bando, Y., Golberg, D.: Functionalized hexagonal boron nitride nanomaterials: emerging properties and applications. Chem. Soc. Rev. **45**, 3989 (2016)
18. Lehtinen, O., Dumur, E., Kotakoski, J., Krasheninnikov, A.V., Nordlund, K., Keinonen, J.: Production of defects in hexagonal boron nitride monolayer under ion irradiation. Nucl. Instrum. Methods Phys. Res. Sect. B Beam Interact. Mater. Atoms. **269**, 1327–1331 (2011)
19. Guo, N., Wei, J., Jia, Y., Sun, H., Wang, Y., Zhao, K., Shi, X., Zhang, L., Li, X., Cao, A., Zhu, H., Wang, K., Wu, D.: Fabrication of large area hexagonal boron nitride thin films for bendable capacitors. Nano Res. **6**, 602–610 (2013)
20. Wu, W., Wang, L., Li, Y., Zhang, F., Lin, L., Niu, S., Chenet, D., Zhang, X., Hao, Y., Heinz, T.F., Hone, J., Wang, Z.L.: Piezoelectricity of single-atomic-layer MoS 2 for energy conversion and piezotronics. Nature **514**, 470–474 (2014)
21. Brennan, C.J., Ghosh, R., Koul, K., Banerjee, S.K., Lu, N., Yu, E.T.: Out-of-Plane electromechanical response of monolayer molybdenum disulfide measured by piezoresponse force microscopy. Nano Lett. **17**, 5464 (2017)
22. Bernardini, F., Fiorentini, V., Vanderbilt, D.: Spontaneous polarization and piezoelectric constants of III-V nitrides. Phys. Rev. B Condens. Matter Mater. Phys. **56**, R10024–R10027 (1997)
23. Ahmadpoor, F., Sharma, P.: Flexoelectricity in two-dimensional crystalline and biological membranes. Nanoscale **7**, 16555 (2015)
24. Mele, E.J., Král, P.: Electric polarization of heteropolar nanotubes as a geometric phase. Phys. Rev. Lett. **88**, 568031–568034 (2002)
25. Sai, N., Mele, E.J.: Microscopic theory for nanotube piezoelectricity. Phys. Rev. B - Condens. Matter Mater. Phys. **68**, 241405 (2003)
26. López-Suárez, M., Pruneda, M., Abadal, G., Rurali, R.: Piezoelectric monolayers as nonlinear energy harvesters. Nanotechnology **25**, 175401 (2014)
27. Dumitrică, T., Landis, C.M., Yakobson, B.I.: Curvature-induced polarization in carbon nanoshells. Chem. Phys. Lett. **360**, 182–188 (2002)
28. Kalinin, S.V., Meunier, V.: Electronic flexoelectricity in low-dimensional systems. Phys. Rev. B Condens. Matter Mater. Phys. **77**, 00340 (2008)
29. Duerloo, K.A.N., Reed, E.J.: Flexural electromechanical coupling: A nanoscale emergent property of boron nitride bilayers. Nano Lett. **13**, 1681–1686 (2013)
30. Kvashnin, A.G., Sorokin, P.B., Yakobson, B.I.: Flexoelectricity in carbon nanostructures: Nanotubes, fullerenes, and nanocones. J. Phys. Chem. Lett. **6**, 2740–2744 (2015)
31. Chatzopoulos, A., Beck, P., Roth, J., Trebin, H.R.: Atomistic modeling of flexoelectricity in periclase. Phys. Rev. B. **93**, 024105 (2016)
32. Kundalwal, S.I., Meguid, S.A., Weng, G.J.: Strain gradient polarization in graphene. Carbon N. Y. **117**, 462–472 (2017)
33. Zhuang, X., He, B., Javvaji, B., Park, H.S.: Intrinsic bending flexoelectric constants in two-dimensional materials. Phys. Rev. B. **99**, 054105 (2019)

34. Barani, E., Korznikova, E.A., Chetverikov, A.P., Zhou, K., Dmitriev, S.V.: Gap discrete breathers in strained boron nitride. Phys. Lett. Sect. A Gen. At. Solid State Phys. **381**, 3553–3557 (2017)
35. Baimova, J.A.: Property control by elastic strain engineering: Application to graphene. J. Micromech. Mol. Phys. **02**, 1750001 (2017)
36. Kundalwal, S.I., Choyal, V.: Enhancing the piezoelectric properties of boron nitride nanotubes through defect engineering. Phys. E Low-dimens. Syst. Nanostruct. **125**, 114304 (2021)
37. Evazzade, I., Lobzenko, I., Golubev, O., Korznikova, E.: Two-phase tension of a carbon nanotube. J. Micromech. Mol. Phys. **05**, 2050001 (2020)
38. Wang, Z.: Alignment of graphene nanoribbons by an electric field. Carbon N. Y. **47**, 3050 (2009)
39. Scarpa, F., Adhikari, S., Gil, A.J., Remillat, C.: The bending of single layer graphene sheets: the lattice versus continuum approach. Nanotechnology **21**, 125702 (2010)
40. Ma, T., Li, B., Chang, T.: Chirality- and curvature-dependent bending stiffness of single layer graphene. Appl. Phys. Lett. **99**, 201901 (2011)
41. Thomas, S., Ajith, K.M., Valsakumar, M.C.: Directional anisotropy, finite size effect and elastic properties of hexagonal boron nitride. J. Phys. Condens. Matter. **28**, 295302 (2016)
42. González, R.I., Valencia, F.J., Rogan, J., Valdivia, J.A., Sofo, J., Kiwi, M., Munoz, F.: Bending energy of 2D materials: Graphene, MoS2 and imogolite. RSC Adv. **8**, 4577 (2018)
43. Wang, S., Chen, Q., Wang, J.: Optical properties of boron nitride nanoribbons: Excitonic effects. Appl. Phys. Lett. **99**, 063114 (2011)
44. Zhang, J.: Piezoelectrically tunable resonance properties of boron nitride nanotube based resonators. J. Appl. Phys. **124**, 055103 (2018)
45. Kundalwal, S.I., Choyal, V.K., Choyal, V., Nevhal, S.K., Luhadiya, N.: Enhancement of piezoelectric and flexoelectric response of boron nitride sheet superlattices via interface and defect engineering. Phys. E Low-dimens. Syst. Nanostruct. **127**, 114563 (2021)
46. Zhao, C., Xu, Z., Wang, H., Wei, J., Wang, W., Bai, X., Wang, E.: Carbon-doped boron nitride nanosheets with ferromagnetism above room temperature. Adv. Funct. Mater. **15**, 5985–5992 (2014)
47. Eshkalak, K.E., Sadeghzadeh, S., Jalaly, M.: Mechanical properties of defective hybrid graphene-boron nitride nanosheets: a molecular dynamics study. Comput. Mater. Sci. **149**, 170–181 (2018)
48. Bhattacharya, A., Bhattacharya, S., Das, G.P.: Band gap engineering by functionalization of BN sheet. Phys. Rev. B - Condens. Matter Mater. Phys. **85**, 035415 (2012)
49. Gao, M., Adachi, M., Lyalin, A., Taketsugu, T.: Long range functionalization of h-BN monolayer by carbon doping. J. Phys. Chem. **120**, 1599C (2016)
50. Zhang, Y.Y., Pei, Q.X., Liu, H.Y., Wei, N.: Thermal conductivity of a h-BCN monolayer. Phys. Chem. Chem. Phys. **19**, 27326–27331 (2017)
51. Beniwal, S., Hooper, J., Miller, D.P., Costa, P.S., Chen, G., Liu, S.Y., Dowben, P.A., Sykes, E.C.H., Zurek, E., Enders, A.: Graphene-like Boron–Carbon–Nitrogen Monolayers. ACS Nano **11**, 2486–2493 (2017)
52. Thomas, S., Lee, S.U.: Atomistic insights into the anisotropic mechanical properties and role of ripples on the thermal expansion of h-BCN monolayers. RSC Adv. **9**, 1238–1246 (2019)
53. Xia, X., Weng, G.J., Zhang, J., Li, Y.: The effect of temperature and graphene concentration on the electrical conductivity and dielectric permittivity of graphene–polymer nanocomposites. Acta Mech. **231**, 1305–1320 (2020)
54. Xia, X., Du, Z., Zhang, J., Li, J., Weng, G.J.: A hierarchical scheme from nano to macro scale for the strength and ductility of graphene/metal nanocomposites. Int. J. Eng. Sci. **162**, 103476 (2021)
55. Kundalwal, S.I.: Review on micromechanics of nano- and micro-fiber reinforced composites. Polym. Compos. **39**, 4243–4274 (2018)
56. Yan, H., Tang, Y., Su, J., Yang, X.: Enhanced thermal-mechanical properties of polymer composites with hybrid boron nitride nanofillers. Appl. Phys. A Mater. Sci. Process. **114**, 331–337 (2014)
57. Sutter, P., Cortes, R., Lahiri, J., Sutter, E.: Interface formation in monolayer graphene-boron nitride heterostructures. Nano Lett. **12**, 4869–4874 (2012)
58. Plimton, S.: Fast Parallel Algorithms for Short-Range Molecular Dynamics. J. Comput. Phys. **117**, 1–19 (1995)
59. Stukowski, A.: Visualization and analysis of atomistic simulation data with OVITO-the open visualization tool. Model. Simul. Mater. Sci. Eng. **18**, 015012 (2010)
60. Tersoff, J.: Modeling solid-state chemistry: Interatomic potentials for multicomponent systems. Phys. Rev. B. **39**, 5566–5568 (1989)
61. Abadi, R., Uma, R.P., Izadifar, M., Rabczuk, T.: Investigation of crack propagation and existing notch on the mechanical response of polycrystalline hexagonal boron-nitride nanosheets. Comput. Mater. Sci. **131**, 86 (2017)
62. Matsunaga, K., Fisher, C., Matsubara, H.: Tersoff potential parameters for simulating cubic boron carbonitrides. Jpn J. Appl. Phys. Part 2 Lett. **39**, 48–51 (2000)
63. KInacI, A., Haskins, J.B., Sevik, C., ÇağIn, T.: Thermal conductivity of nanostructures. Phys. Rev. **86**, 115410 (2012)
64. Han, T., Luo, Y., Wang, C.: Effects of temperature and strain rate on the mechanical properties of hexagonal boron nitride nanosheets. J. Phys. D. Appl. Phys. **47**, 025303 (2014)
65. Amalia, W., Nurwantoro, P., Sholihun: Sholihun: density-functional-theory calculations of structural and electronic properties of vacancies in monolayer hexagonal boron nitride (h-BN). Comput. Condens. Matter. **18**, e00354 (2019)
66. Kundalwal, S.I., Choyal, V.K., Luhadiya, N., Choyal, V.: Effect of carbon doping on electromechanical response of boron nitride nanosheets. Nanotechnology **31**, 405710 (2020)
67. Dewapriya, M.A.N., Rajapakse, R.K.N.D., Phani, A.S.: Atomistic and continuum modelling of temperature-dependent fracture of graphene. Int. J. Fract. **187**, 199 (2014)
68. Kundalwal, S.I., Choyal, V.: Transversely isotropic elastic properties of carbon nanotubes containing vacancy defects using MD. Acta Mech. **229**, 2571–2584 (2018)

69. Choyal, V., Kundalwal, S.I.: Effect of Stone-Wales defects on the mechanical behavior of boron nitride nanotubes. Acta Mech. **231**, 4003–4018 (2020)
70. Evans, D.J., Holian, B.L.: The Nose-Hoover thermostat. J. Chem. Phys. **83**, 4069 (1985)
71. Choyal, V., Choyal, V.K., Kundalwal, S.I.: Effect of atom vacancies on elastic and electronic properties of transversely isotropic boron nitride nanotubes: A comprehensive computational study. Comput. Mater. Sci. **156**, 332–345 (2019)
72. Tan, D., Willatzen, M., Wang, Z.L.: Out-of-plane polarization in bent graphene-like zinc oxide and nanogenerator applications. Adv. Funct. Mater. **30**, 1907885 (2020)
73. Tan, D., Willatzen, M., Wang, Z.L.: Prediction of strong piezoelectricity in 3R-MoS2 multilayer structures. Nano Energy **56**, 512 (2019)
74. Xiong, S., Cao, G.: Molecular dynamics simulations of mechanical properties of monolayer MoS2. Nanotechnology **27**, 105701 (2015)
75. Javvaji, B., He, B., Zhuang, X., Park, H.S.: High flexoelectric constants in Janus transition-metal dichalcogenides. Phys. Rev. Mater. **3**, 125402 (2019)
76. Li, C., Wang, Z., Li, F., Rao, Z., Huang, W., Shen, Z., Ke, S., Shu, L.: Large flexoelectric response in PMN-PT ceramics through composition design. Appl. Phys. Lett. **115**, 142901 (2019)
77. Wirtz, L., Rubio, A.: The phonon dispersion of graphite revisited. Solid State Commun. **63**, 045425 (2004)
78. Moon, W.H., Hwang, H.J.: Molecular mechanics of structural properties of boron nitride nanotubes. Phys. E Low-Dimens. Syst. Nanostruct. **23**, 26–30 (2004)
79. Duerloo, K.A.N., Ong, M.T., Reed, E.J.: Intrinsic piezoelectricity in two-dimensional materials. J. Phys. Chem. Lett. **13**, 1681 (2012)
80. Beheshtian, J., Sadeghi, A., Neek-Amal, M., Michel, K.H., Peeters, F.M.: Induced polarization and electronic properties of carbon-doped boron nitride nanoribbons. Phys. Rev. B - Condens. Matter Mater. Phys. **86**, 195433 (2012)
81. Ansari, R., Mirnezhad, M., Sahmani, S.: Prediction of chirality- and size-dependent elastic properties of single-walled boron nitride nanotubes based on an accurate molecular mechanics model. Superlattices Microstruct. **80**, 196 (2015)
82. Thomas, S., Ajith, K.M., Chandra, S., Valsakumar, M.C.: Temperature dependent structural properties and bending rigidity of pristine and defective hexagonal boron nitride. J. Phys. Condens. Matter. **27**, 315302 (2015)
83. Gao, E., Xu, Z.: Thin-shell thickness of two-dimensional materials. J. Appl. Mech. Trans. ASME. **82**, 121012 (2015)
84. Kang, S., Jeon, S., Kim, S., Seol, D., Yang, H., Lee, J., Kim, Y.: Tunable out-of-plane piezoelectricity in thin-layered MoTe2 by surface corrugation-mediated flexoelectricity. ACS Appl. Mater. Interfaces. **10**, 27424–27431 (2018)